

Article

Vital Role of Synthesis Temperature in Co–Cu Layered Hydroxides and Their Fenton-like Activity for RhB Degradation

Ruixue Zhang, Yanping Liu, Xinke Jiang and Bo Meng *

Department of Engineering Research Center of Advanced Functional Material Manufacturing of Ministry of Education, Zhengzhou University, Zhengzhou 450001, China; zrx3066@163.com (R.Z.); lyp2423821591@gs.zzu.edu.cn (Y.L.); xinke7955@163.com (X.J.)

* Correspondence: mengbo8305@zzu.edu.cn

Abstract: Cu and Co have shown superior catalytic performance to other transitional elements, and layered double hydroxides (LDHs) have presented advantages over other heterogeneous Fenton catalysts. However, there have been few studies about Co–Cu LDHs as catalysts for organic degradation via the Fenton reaction. Here, we prepared a series of Co–Cu LDH catalysts by a co-precipitation method under different synthesis temperatures and set Rhodamine B (RhB) as the target compound. The structure–performance relationship and the influence of reaction parameters were explored. A study of the Fenton-like reaction was conducted over Co–Cu layered hydroxide catalysts, and the variation of synthesis temperature greatly influenced their Fenton-like catalytic performance. The Co–Cu_{t=65°C} catalyst with the strongest LDH structure showed the highest RhB removal efficiency (99.3% within 30 min). The change of synthesis temperature induced bulk-phase transformation, structural distortion, and metal–oxygen (M–O) modification. An appropriate temperature improved LDH formation with defect sites and lengthened M–O bonds. Co–Cu LDH catalysts with a higher concentration of defect sites promoted surface hydroxide formation for H₂O₂ adsorption. These oxygen vacancies (Ovs) promoted electron transfer and H₂O₂ dissociation. Thus, the Co–Cu LDH catalyst is an attractive alternative organic pollutants treatment.

Keywords: Cu–Co LDH; oxygen vacancy; hydroxyl radicals; RhB; Fenton-like reaction



Citation: Zhang, R.; Liu, Y.; Jiang, X.; Meng, B. Vital Role of Synthesis Temperature in Co–Cu Layered Hydroxides and Their Fenton-like Activity for RhB Degradation. *Catalysts* **2022**, *12*, 646. <https://doi.org/10.3390/catal12060646>

Academic Editors: Gassan Hodaifa, Antonio Zuorro, Joaquín R. Dominguez, Juan García Rodríguez, José A. Peres and Zacharias Frontistis

Received: 5 May 2022
Accepted: 3 June 2022
Published: 13 June 2022

Publisher's Note: MDPI stays neutral with regard to jurisdictional claims in published maps and institutional affiliations.



Copyright: © 2022 by the authors. Licensee MDPI, Basel, Switzerland. This article is an open access article distributed under the terms and conditions of the Creative Commons Attribution (CC BY) license (<https://creativecommons.org/licenses/by/4.0/>).

1. Introduction

Rhodamine B (RhB) is a cationic xanthene dye with an aromatic structure and persistent stability. It is commonly used in the printing and dyeing industries [1]. However, it is harmful if swallowed by human beings and animals, and causes irritation to the skin, eyes, gastrointestinal tract, and respiratory tract [1]. Furthermore, it also causes phototoxic and photoallergic reactions. The carcinogenicity, reproductive and developmental toxicity, neurotoxicity, and chronic toxicity to humans and animals have been experimentally proven [2]. Therefore, the insufficient disposal of RhB-containing wastewater can lead to severe environmental problems and threaten human health. Many methods have been developed for dye wastewater treatment, such as adsorption [3,4], advanced oxidation [5–8], biological treatment [9,10], and photodegradation [11,12].

Among advanced oxidation processes (AOPs), the Fenton reaction has drawn great attention from the academic and industrial fields as an effective wastewater treatment owing to its low operating cost, low toxicity, and high degradation efficiency [13,14]. However, the homogeneous Fenton reaction has disadvantages, like a narrow working pH range, poor recyclability, and secondary pollution of residual sludge [15,16]. To overcome these drawbacks, the heterogeneous Fenton-like reaction with better stability and recyclability has been promoted as a promising alternative to the decomposition of refractory organics. Moreover, Cu and Co have exhibited superior catalytic performance to other transitional elements, so they have attracted a lot of research attention in the field of Fenton reaction [17–21].

Owing to their unique layered structure, layered double hydroxides (LDHs) have presented clear advantages over other heterogeneous Fenton catalysts, with negligible metal leaching during the reaction [22–24]. The LDH is a two-dimensional (2D) layered hydroxide formulated as $[M^{2+}_{1-x}M^{3+}_x(OH)_2]^{x+}(A^{n-})_{x/n} \cdot mH_2O$, in which M^{2+} and M^{3+} represent divalent and trivalent cations in the host layers, respectively, and A^{n-} stands for the compensative anion in the interlayer [25]. Moreover, abundant alkaline sites in the LDH structure can benefit the maintenance of a weak alkaline condition during reaction, which greatly depresses the leaching condition of catalysts [26,27]. Moreover, the metal component in the positive layer with low redox potential, such as Cu, Fe, Ni, and Co, can favor the electron transfer in reaction [28]. Furthermore, the oxygen vacancies (Ovs) with rich electrons can stretch the O–O bond in H_2O_2 after adsorption and thus facilitate the production of $\cdot OH$ [29–31] with accelerated degradation of organics. In recent years, Cu-containing LDHs have drawn great attention among LDH catalysts for Fenton-like reactions. Wang et al. prepared the $Cu_1Ni_2Sn_{0.75}$ LDH catalyst with almost total (97.8%) phenol mineralization with a neutral pH value [32]. Tao et al. fabricated Cu–Fe LDHs to treat methyl orange, with a nearly 100% removal in 13.5 min [33]. A Cu–Zn–Fe LDH was also developed for the decomposition of an acetaminophen-containing sample, with a degradation efficiency up to 100% within 24 h [34]. However, there have been few studies on Co–Cu LDHs as catalysts for organic degradation via the Fenton reaction.

In this work, we prepared a series of Co–Cu LDH catalysts by a co-precipitation method under different synthesis temperatures and set RhB as the target compound. In addition, the structure–performance relationship and the influence of reaction parameters were also explored.

2. Results

2.1. Bulk-Phase and Electronic Structure Characterization

Nitrogen adsorption–desorption isotherms of all catalysts are displayed in Figure 1a. The isotherms show that all catalysts possessed the typical IV type isotherms with obvious hysteresis loops at high relative pressures ($0.6 < P/P_0 < 1$), indicating the presence of mesopores. Meanwhile, there were almost no micropores in the samples, as there was little N_2 adsorption for all catalysts at low relative pressures ($P/P_0 < 0.1$), which can also be clearly observed from the pore size distribution curves (Figure 1b). In addition, as shown in Table 1, the specific surface area of the catalysts decreased with increased synthesis temperature, to 65 °C, yet it exhibited slightly increasing return when the synthesis temperature reached 75 °C and 85 °C. A larger specific surface area usually provides more active sites, yet it had little relationship with the catalytic activity in this case, as $Co-Cu_{t=65^\circ C}$ exhibited the highest RhB removal with the smallest surface area. In addition, the catalysts had a higher specific surface area, which often exists in more active sites, and the specific surface area of the catalyst synthesized at 65 °C was the smallest. The result indicates that the structure of the catalyst is sensitive to the synthesis temperature. Furthermore, according to the experimental results of ICP and XPS (Table 1), the molar ratio of copper and cobalt elements in the catalyst is about 4.15 and 4.2, respectively, which were very close to the theoretical value of 4 for the molar ratio of copper and cobalt elements.

Table 1. BET surface area, BJH mean pore size, pore volume, and elemental composition of catalysts.

Sample	S_{BET} ($m^2 g^{-1}$)	Volume ($cm^3 g^{-1}$)	Pore Size (nm)	Co:Cu Molar Ratio	Surface Co:Cu Molar Ratio
$Cu-Co_{t=45^\circ C}$	65.99	0.32	13.96	4.12	4.4
$Cu-Co_{t=55^\circ C}$	62.86	0.36	17.52	4.15	4.3

Table 1. Cont.

Sample	S_{BET} ($\text{m}^2 \text{g}^{-1}$)	Volume ($\text{cm}^3 \text{g}^{-1}$)	Pore Size (nm)	Co:Cu Molar Ratio	Surface Co:Cu Molar Ratio
Cu–Co _{t=65°C}	46.47	0.22	13.38	4.14	4.2
Cu–Co _{t=75°C}	57.33	0.32	17.19	4.14	4.1
Cu–Co _{t=85°C}	60.33	0.36	17.26	4.1	4.3

The Co:Cu molar ratio was analyzed by ICP, the surface Co:Cu Molar ratio was analyzed by XPS.

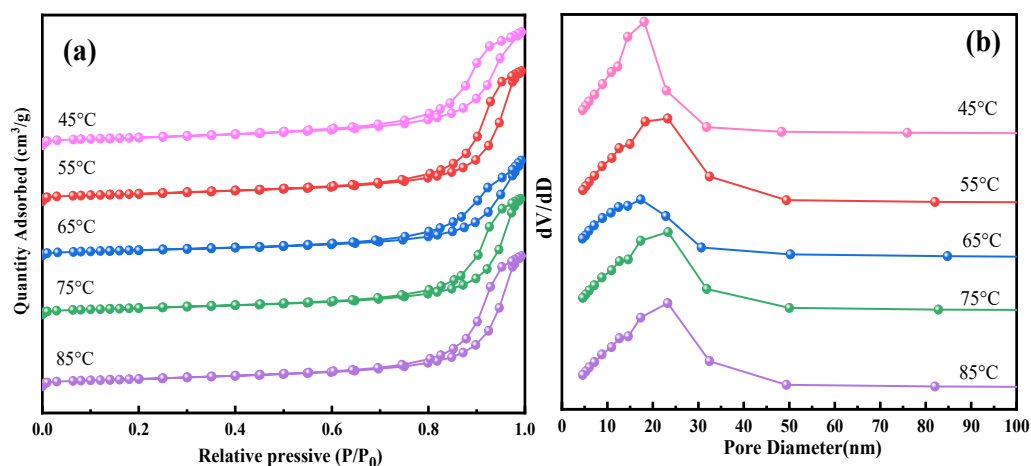


Figure 1. (a) N_2 adsorption/desorption isotherms and (b) pore size distribution curves of catalysts.

The bulk-phase structure of catalysts was further studied by XRD analysis. As shown in Figure 2a, when the synthesis temperature was in the range of 45–75 °C, all catalysts exhibited a group of characteristic diffractions corresponding to (003), (006), (012), and (015) crystalline planes of the hydrotalcite-like (JCPDS#35-0965) structure at 2θ of 11.7, 23.4, 33.7, and 39.1, respectively [35]. The basal spacing $d(003)$ around 0.74 nm was in line with the presence of carbonate in the interlayer space, as in previous reports [25]. Moreover, a second phase was $\text{Cu}(\text{OH})_2$ (JCPDS#80-0656) owing to the excessive Cu existence besides the necessary composition for LDH or the Jahn-Teller effect. This is because Cu^{2+} could be situated in near-lying octahedra with the formation of the copper compound with distorted octahedra, which is energetically preferred to the compound of LDH [25]. A higher synthesis temperature would enhance the crystallinity of the LDH structure, with an improved intensity of (003) reflection in the range of 45–65 °C. This may be highly related to the promoted oxidation of Co^{2+} , which resulted in the improved LDH structure with increasing temperature. However, the condition for Co–Cu_{t=75°C} inverted for the decomposition of LDH framework under the circumstances. When the synthesis temperature was 85 °C, the LDH structure of the catalyst disappeared. Thus, the Co–Cu_{t=65°C} catalyst had a better LDH structure. As shown in Figure 3, the catalyst presented sheet-like structures, as is typical for LDH materials.

FT-IR characterization was then carried out to investigate the special Co–Cu interaction, LDH property, and their influence on catalytic performance. The patterns in Figure 2b show some vibrational information of different catalyst structures. There are three types of O–H stretching modes in the catalysts. One is the $\nu_{\text{O-H}}$ vibration of the metal hydroxide located at about 3570 cm^{-1} and 3623 cm^{-1} for $\text{Cu}(\text{OH})_2$ and $\text{Co}(\text{OH})_2$, respectively [36]. Another broad band in the region of 3300–3500 cm^{-1} can be attributed to the O–H stretching of the adsorbed and interlayer water [25]. Furthermore, the weak band at 1634 cm^{-1} was associated with the hydroxyl deformation mode of the water molecules in the interlayer [37]. In addition, the peaks at c.a. 1361 cm^{-1} , 992 cm^{-1} , and 683 cm^{-1} can be attributed to different stretching modes of carbonate [25], indicating carbonates as the primary compensating anions in the LDH interlayer, which is in line with XRD results.

Moreover, the peaks located below 683 cm^{-1} were related to M–O vibrations ($M = \text{Co}$ and/or Cu) [36], which varied across samples, indicating that the different M–O bonds may determine their corresponding catalytic performance.

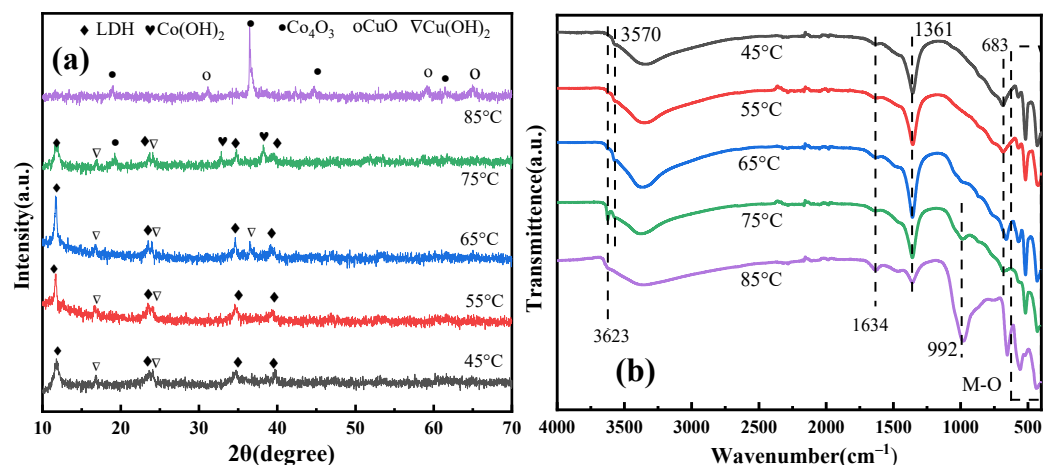


Figure 2. (a) XRD patterns of catalysts; (b) FT-IR spectra of catalysts.

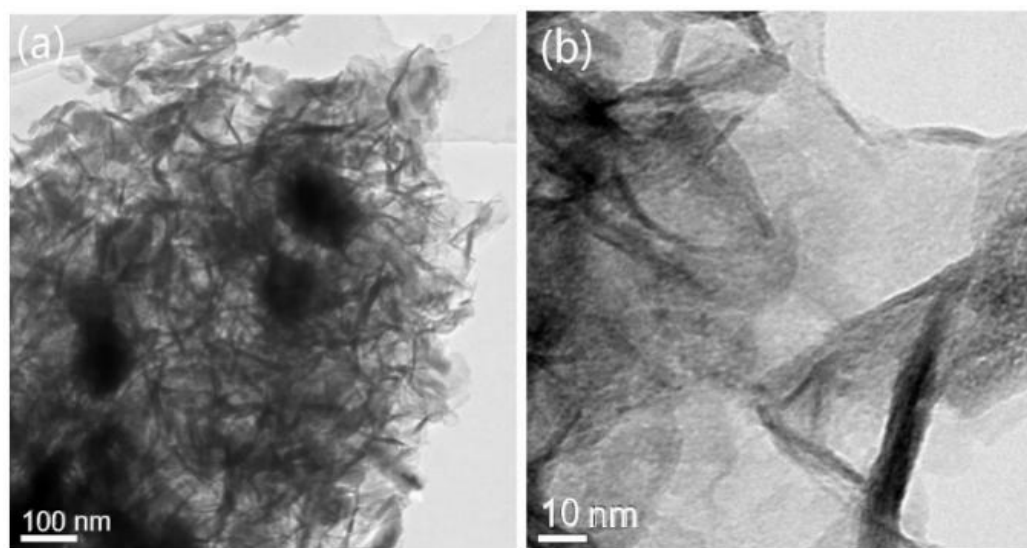


Figure 3. TEM images of $\text{Co-Cu}_{t=65^\circ\text{C}}$ catalyst (a) larger-scale image (b) small-scale image.

Raman spectra analysis was further conducted to investigate these M–O bonds' properties. As shown in Figure 4a, the four vibrational modes exhibited at ca. 189 , 461 , 527 , and 688 cm^{-1} all belonged to cobalt oxides corresponding to F_{2g}^1 , E_g , F_{2g}^2 , and A_{1g} species, respectively [38–40], and no Cu-related peaks were detected in all catalysts. In particular, the shifts for E_g suggested that this is probably related to the incorporation of Cu in the Co-related lattice. Specifically, the bands at 688 cm^{-1} (A_{1g}) and 189 cm^{-1} (F_{2g}^1) could be assigned to the Raman vibration of $\text{Co}^{3+}\text{-O}^{2-}$ at octahedral sites and $\text{Co}^{2+}\text{-O}^{2-}$ at tetrahedral sites, respectively [41]. The bands at 461 cm^{-1} (E_g) and 527 cm^{-1} (F_{2g}^2) can be attributed to the combined vibrations in tetrahedral sites and octahedral oxygen motions [42]. Particularly, the band of 527 cm^{-1} can be ascribed to Co-related doubly occupied Ovs bound with donor defects [43]. According to our previous study, the band's peak intensity was positive to the concentration of surface Ovs. With the improved LDH crystallinity and peak intensity, shown in Figure 4a, F_{2g}^2 modes exhibited the same enhanced tendency, indicating an increasing Ov density.

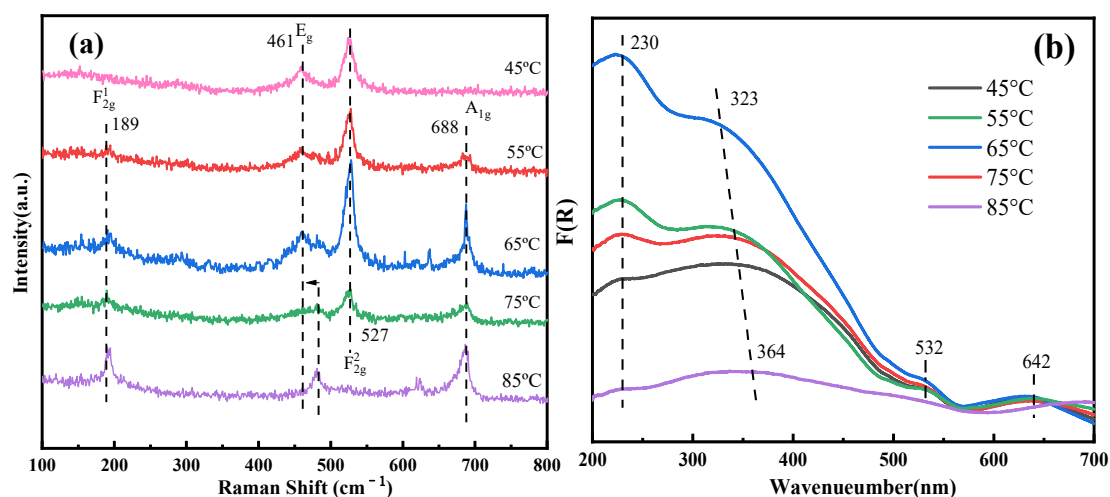


Figure 4. (a) Raman spectra of catalysts; (b) UV-Vis DRS spectra of catalysts.

As shown in Figure 5, the convolutions of O1s XPS spectra were carried out for detailed information, especially for oxygen defects. The core level spectra were fitted into three identified peaks. Peaks at 529.8 and 530.6 eV were attributed to oxygen atoms bound to lattice oxygen for metal oxides and hydroxyl species, respectively [31]. It is noted that the peak at ca. 533.4 eV can be ascribed to the presence of defect sites in the low oxygen-coordination [44]. In addition, Co-Cu_{t=65°C} presented the highest defect density (Table 2), with its changing agreeing well with the Raman analysis.

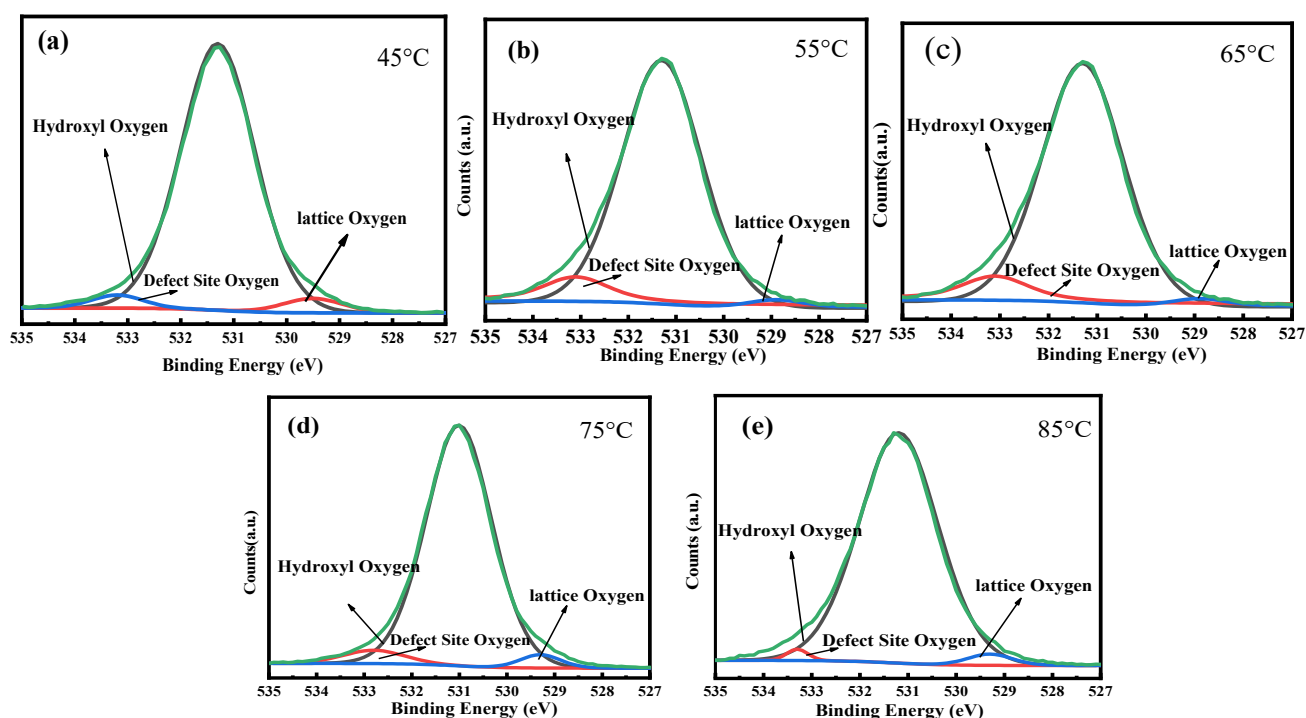


Figure 5. O1s XPS spectra of catalysts. (a) Co-Cu_{t=45°C}; (b) Co-Cu_{t=55°C}; (c) Co-Cu_{t=65°C}; (d) Co-Cu_{t=75°C}; (e) Co-Cu_{t=85°C}.

Table 2. Oxygen defect density of catalysts.

Sample	Oxygen Defect Density (%)	O1s BE for Defect Sites (eV)
Cu–Co _{t=45°C}	5.6	533.2
Cu–Co _{t=55°C}	7.8	533.1
Cu–Co _{t=65°C}	12.8	533.8
Cu–Co _{t=75°C}	9.2	533.7
Cu–Co _{t=85°C}	3.19	532.3

The density of defects was calculated by atomic ratio depending on the area percentage of defect site oxygen in total area for all peaks from XPS.

UV-Vis DRS spectra (Figure 4b) shed more light on the special electronic property of Ov and the LDH structure. The absorption peak observed at 230 nm can be attributed to ligand-to-metal charge-transfer excitations occurring in the MO₆ coordination [45]. Moreover, the peaks at c.a. 323–364 nm and 642 nm can be associated with O²⁻ → Co²⁺ and O²⁻ → Co³⁺, respectively [41,46,47]. The shifts of the peaks also depicted the different doping conditions of Cu in the LDH structure for different catalysts. In addition, the distinctive peak at 532 nm is related to the special metal–metal charge transfer of the Co–O–Cu oxo-bridge in the MO₆ environment for LDH, as it included the transitions of d_{z²} → d_{x²-y²} for Cu²⁺, ¹A_{1g} → ¹T_{1g} for Co³⁺, and ⁴T_{1g}(F) → ⁴T_{1g}(P) for Co²⁺ with weak-field ligands [48–51], which is also related to the generation of surface Ov, according to previous publications [52]. A stronger peak intensity suggested a higher Ov concentration, with its changing agreeing well with the Raman analysis. Thus, it can be concluded from the above discussion that improved LDH structure is likely to possess more Co–O–Cu oxo-bridge interaction with more lattice disorder resulting from the incorporation of Cu in Co sites. This special Co–O–Cu structure can promote the generation of surface Ov, which is positively related to the catalytic performance [35,41].

2.2. Catalytic Performance

The catalytic activity for all catalysts with different synthesis temperatures are shown in Figure 6a. The RhB removal was raised from 82.5% to 99.3% as the fabricated temperature increased from 45 °C to 65 °C, respectively. However, a further increment in the synthesis temperature to 75 °C and 85 °C decreased the RhB degradation efficiency to 85.10% and 65.99%, respectively. Moreover, the adsorption only counted for less than 10% of the total removal without the addition of H₂O₂, indicating that self-decomposition and/or adsorption of RhB by catalysts can be excluded in this case, and the Fenton oxidation is the key factor for total organic elimination. The homogeneous Fenton test showed that the degradation resulting from metal leaching only contributed 9.3% of the total removal from the homogeneous part (Figure 6b). Furthermore, the quenching experiment showed that ·OH was the main reactive oxygen species of the reaction, as the RhB removal declined to 9.8% with the existence of a scavenger (Figure 6c). Thus, the RhB decomposition can be mostly ascribed to the ·OH generation over the catalyst surface rather than ·OH produced by leaching metals.

The results of the catalytic performance tests reveal that the synthesis temperature had a great impact on catalytic activity, as the optimum synthesis temperature of the catalyst was 65 °C. However, the Co–Cu_{t=65°C} LDH catalyst had the smallest specific surface areas in the BET analysis, indicating that the catalyst performance is more structurally dependent than the surface area in the Fenton-like reaction. In addition, among other catalysts, the Co–Cu_{t=65°C} LDH catalyst had the best performance, which can be attributed to its excellent LDH structure and high density of Ov based on the XRD and Raman analyses. According to a previous study [35], Ov is the main active site of the LDH structure, and it promotes H₂O₂ adsorption, electron transfer, and H₂O₂ dissociation during reaction, which benefit the generation of effective ·OH. In addition, the Co–Cu_{t=65°C} LDH catalyst exhibited better RhB removal efficiency compared with other catalysts (Table 3). Therefore, we selected the Co–Cu_{t=65°C} LDH catalyst to carry out the following experiments.

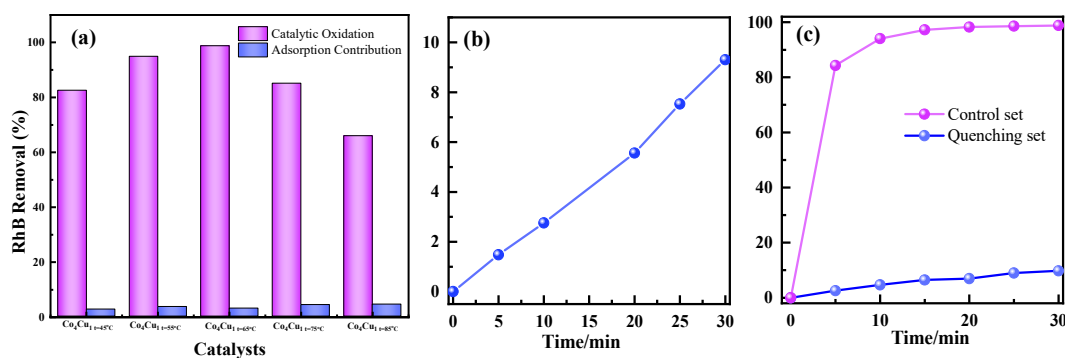


Figure 6. (a) Catalytic performance of catalysts; (b) homogeneous RhB degradation for Co–Cu_{t=65°C} with $C_{Cu^{2+}} = 0.072$ ppm and $C_{Co^{2+}} = 2.814$ ppm according to metal leaching analysis; (c) quenching test for Co–Cu_{t=65°C}.

Table 3. Comparison of RhB removal among different catalysts.

Catalysts	Conditons	Removal	Ref.
Fe/MCM-41	1 g/L catalysts, 20 mM H ₂ O ₂ , 100 ppm RhB, pH = 4.0, 80 °C, 30 min.	99.1%	[53]
MgFe ₂ O ₄	0.625 g/Lcatalysts, 1.00 vol%H ₂ O ₂ , 10 ppm RhB, 45 °C, pH = 6.44, 180 min	90.0%	[54]
Cu/Al ₂ O ₃	1 g/Lcatalyst, 10 ppm RhB, 1000 ppm H ₂ O ₂ , pH = 5.14, 50 °C, 30 min	98.5%	[55]
Fe ₃ O ₄ /MI	0.5 g/Lcatalyst, 20 mM H ₂ O ₂ , 10 ppm RhB, pH = 7, 25 °C, 30 min	99.6%	[56]
Co–Cu LDH	0.1 g/Lcatalyst, 240 ppm H ₂ O ₂ , 10 ppm RhB, pH = 7, 40 °C, 30 min	99.3%	This work

2.3. Investigation of Reaction Parameters

To better understand the reaction process, we also performed condition experiments to investigate the influence of different reaction parameters such as H₂O₂ dosage, reaction temperature, and pH surroundings for RhB removal, and find out the optimum reaction parameters for the catalyst Co–Cu_{t=65°C}. All experiments were carried out in conditions of 100 mL, 10 ppm RHB, 10 mg catalyst, 240 ppm H₂O₂, and 50 °C under 700 rpm-stirring for 60 min with initial pH = 5.15 unless otherwise specified for investigations of each parameter. The kinetic study was based on the first-order reaction in the first 7.5 min to obtain a more satisfactory fitting model.

2.3.1. Effect of Initial H₂O₂ Dosage

The effect of the initial H₂O₂ dosage on degradation of RhB was investigated in the range of 160 to 960 ppm. As shown in Figure 7, as the H₂O₂ dosage rose from 160 to 480 ppm, the RhB removal also improved from 77.71 to 96.19% in 5 min, with its corresponding reaction rate constant k_G (min⁻¹) surging from 0.1924 to 0.4938 min⁻¹ (Table 4). This phenomenon can be ascribed to the fact that the adequate dose-up of initial H₂O₂ can directly promote the generation of ·OH with further improvement for RhB removal [57]. However, a further increase of the initial H₂O₂ dosage to 960 ppm brought about a drop of the catalytic performance, as excessive H₂O₂ and ·OH can quench ·OH and decrease the degradation efficiency [35,55,58].

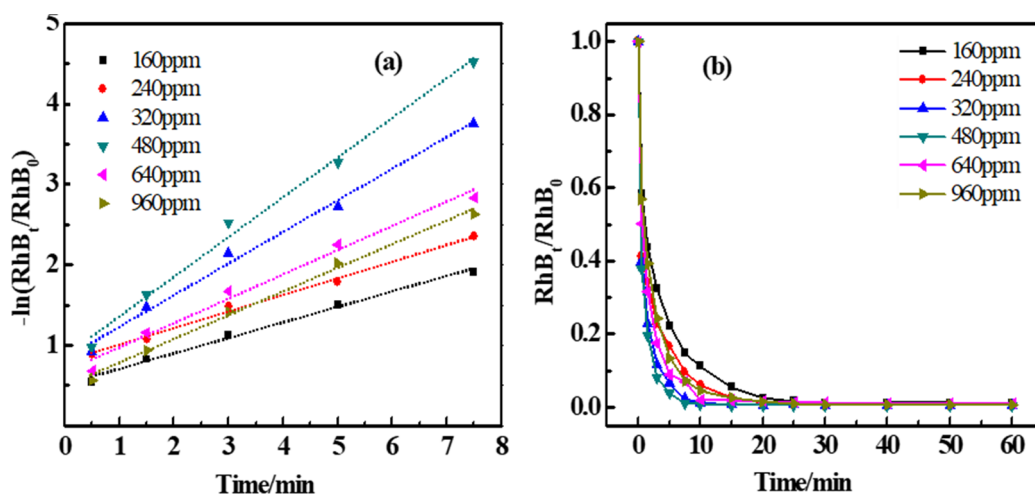


Figure 7. Catalytic degradation of RhB under different H_2O_2 concentration (a) plots of pseudo-first-order kinetics; (b) RhB concentration.

Table 4. The influence of H_2O_2 concentration on k_G for the first 7.5 min and RhB removal in the first 5 min.

H_2O_2 Concentration/ppm	k_G for First 7.5 min (min^{-1})	R_2	RhB Removal in First 5 min (%)
160	0.1924	0.9895	77.7
240	0.2070	0.9928	83.4
320	0.3930	0.9898	93.4
480	0.4938	0.9900	96.2
640	0.3019	0.9795	91.1
960	0.2943	0.9929	86.7

2.3.2. Effect of Reaction Temperature

Figure 8 shows the positive relationship between the reaction temperature and RhB. Specifically, the RhB removal in the first 5 min was 38.09%, 48.93%, 65.55%, and 84.07% with the reaction temperature of 27 °C, 33 °C, 40 °C, and 50 °C, respectively. In addition, the reaction rate constant k also increased with the rise of the reaction temperature (Table 5). This is attributable to the fact that a higher temperature promotes the collision between molecules, in which case more molecules obtain energy exceeding the activation barrier [59]. Thus, the reactions for the generation of $\cdot\text{OH}$ and degradation of RhB were both improved simultaneously.

Table 5. The influence of reaction temperatures on k_G for the first 7.5 min and RhB removal in the first 5 min.

Reaction Temperature/°C	k_G for the First 7.5 min (min^{-1})	R_2	RhB Removal in the First 5 min (%)
27	0.0303	0.9841	38.1
33	0.0628	0.9967	48.9
40	0.1256	0.9915	65.5
50	0.2070	0.9929	84.1

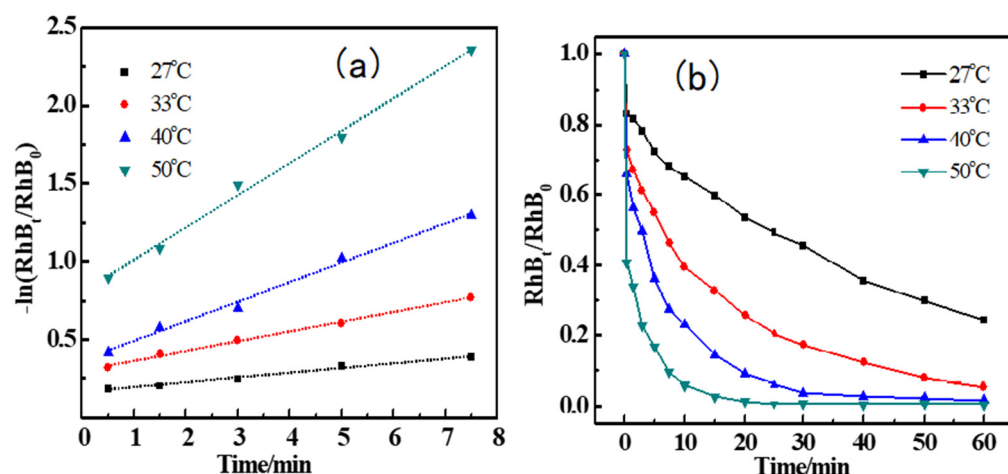


Figure 8. Catalytic degradation of RhB under different reaction temperatures (a) plots of pseudo-first-order kinetics; (b) RhB concentration.

2.3.3. Effect of pH Surroundings

It has been well established that the reaction surroundings, especially for the pH value, play an important role in Fenton or Fenton-like reactions. Thus, HNO₃ and NaOH were used to adjust the initial pH value in this work to better understand its influence on RhB removal. As shown in Figure 9, the catalyst presented excellent performance within 30 min over a wide pH range. Moreover, as the pH value increased from 5.2 to 7.9, the reaction rate constant k_G (Table 6) significantly improved within the first 5 min. In addition, the highest RhB removal of 97.5% was achieved at pH = 7.0. However, a further increase of the pH value had a negative impact on the reaction, with the removal in the first 5 min dropping to 61.7%.

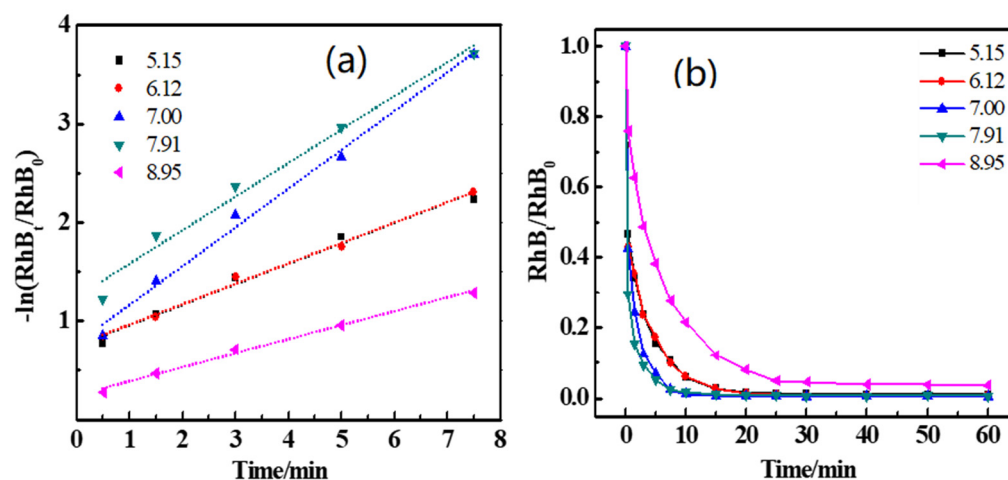


Figure 9. Catalytic degradation of RhB under different pH conditions (a) plots of pseudo-first-order kinetics; (b) RhB concentration.

Table 6. The influence of pH on k_G for the first 7.5 min and RhB removal in the first 5 min.

pH	K_G for the First 7.5 min (min^{-1})	R_2	RhB Removal in the First 5 min (%)
5.15	0.2075	0.9784	84.3
6.12	0.2070	0.9928	82.6
7.00	0.3930	0.9898	93.0
7.91	0.3405	0.9760	94.9
8.95	0.1418	0.9911	61.7

There are a few possible reasons for this phenomenon. In an acidic environment, the greater stability of H_2O_2 [60] and the metal leaching of catalysts lead to a decrease in catalytic activity. However, in strong alkaline solutions, the self-decomposition of H_2O_2 and the side reactions for $\cdot\text{OH}$ scavenging are aggravated with a decline of the oxidation potential for $\cdot\text{OH}/\text{H}_2\text{O}$ [61], which adversely affects the reaction.

2.3.4. The Reusability and Stability of Catalysts

To explore the stability of the $\text{Co-Cu}_{t=65^\circ\text{C}}$ catalyst, repeated experiments of catalyst recycling and reuse were carried out under the same experimental conditions. Experiments were carried out in conditions of 100 mL, 10 ppm RHB, 10 mg catalyst, 240 ppm H_2O_2 , 40 °C under 700 rpm-stirring for 60 min with initial pH = 5.15. As shown in Figure 10a, the efficiency of RhB dye degradation was only slightly decreased after being reused three times, but the removal rate of RhB could still exceed 85% after being reused three times. Hence, the catalysts showed good reusability in catalytic degradation. For the stability, the XRD spectra of $\text{Co-Cu}_{t=65^\circ\text{C}}$ catalyst before and after the third run cycle are depicted in Figure 10b, where the spectra appear identical except for the slightly lower peak intensity of the (003) reflection at 2θ of 11.7, which presented a new $\text{Cu}(\text{OH})_2$ phase after the recycling reaction. This can be attributed to the leaching of metal elements of the $\text{Co-Cu}_{t=65^\circ\text{C}}$ catalyst after three cycles.

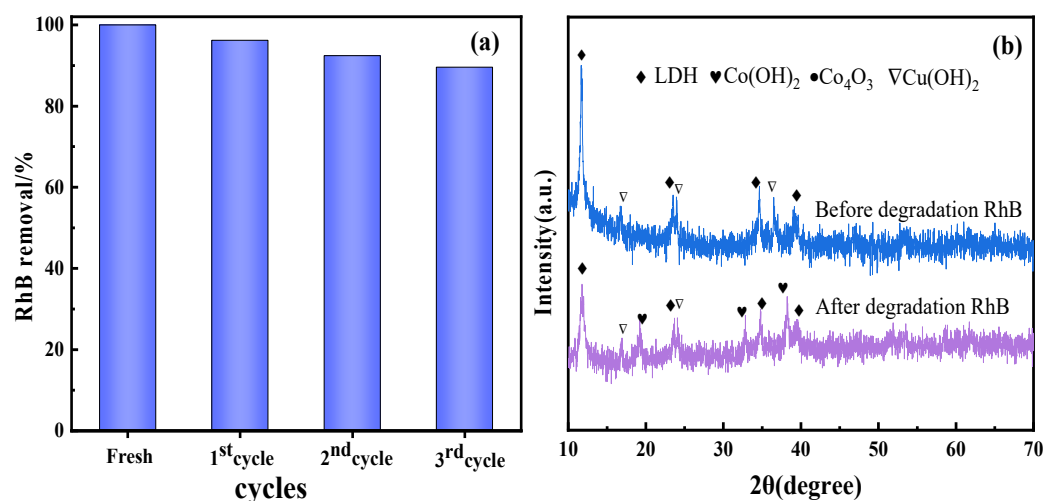
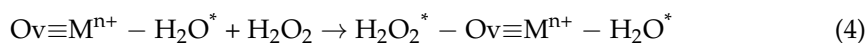
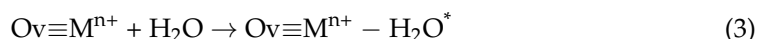
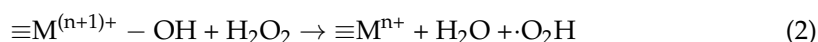


Figure 10. The reusability and stability of $\text{Cu-Co}_{t=65^\circ\text{C}}$ catalyst (a); and XRD diffractograms before and after degradation (b).

2.4. Plausible Mechanism

According to the above experimental results, the possible heterogeneous Fenton-like reaction mechanisms on RhB degradation by the Cu-Co LDH/ H_2O_2 were proposed in Equations (1)–(7). Irrespective of the existence of Oxygen vacancy (Ov), the events of Equations (1) and (2) occurred [62]. Surface active centers of Co and/or Cu are involved in one-electron oxidation to catalyze H_2O_2 to $\cdot\text{OH}$ [30]. Concurrently, $\text{M}^{(n+1)+}$ ($\text{M} = \text{Co}$ and Cu) was reduced by H_2O_2 according to the Haber-Weiss mechanism [63]. When oxygen vacancy co-existed, Equations (1) and (2) accelerated and the steps of Equations (3)–(6) were in effect [62]. Firstly, H_2O adsorbed on the surface vacancy of $\text{Vo}\equiv\text{Mn}^+$ defect sites (Equation (3)) to form the surface hydroxyl group [64]. Secondly, through ligand exchange of the previous surface hydroxyl group which was prior to electron transfer, H_2O_2 adsorbed on the same defect sites [64] (Equation (4)). Thirdly, the existence of Ov stretched of the O–O bond, which facilitated activation of H_2O_2 to produce $\cdot\text{OH}$ (Equation (5)) [21,65,66]. Finally, the reactive radicals ($\cdot\text{OH}$) readily attacked RHB that adsorbed nearby the active sites (Equation (7)):





Therefore, Ov plays a key role in the heterogeneous Fenton-like reaction. The higher the content of Ov in the catalyst, the faster the $\cdot OH$ is generated, which in turn increases the degradation rate of RhB. It can be seen intuitively from Figure 11 that the Co-Cu_{t=65°C} catalyst contains more Ov, and this is also the reason for the better performance of the Co-Cu_{t=65°C} catalyst.

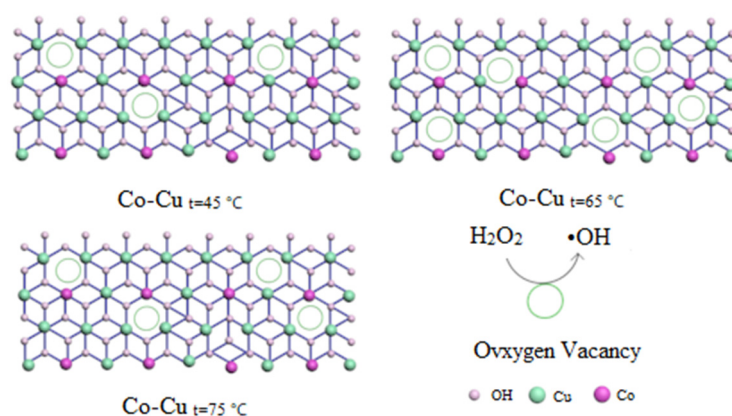


Figure 11. Structural model diagram of catalysts.

3. Materials and Methods

3.1. Catalyst Preparation

Cu-Co LDH catalysts were obtained by the co-precipitation method [25,35]. Specifically, mixed salts of Cu (NO₃)₂·3H₂O and Co (NO₃)₂·6H₂O with a Co/Cu molar ratio of 4:1 was dissolved in 150 mL deionized water. The above solution dropwise added a mixed alkaline of NaOH (0.4 M) and Na₂CO₃ (0.2 M) to adjust the pH to 12 under vigorous magnetic stirring at 25 °C for 1 h. The mixture was aged at different temperatures (45 °C, 55 °C, 65 °C, 75 °C, 85 °C) for 24 h with subsequent centrifugation after being washed by deionized water several times. The obtained pastes were then dried at 60 °C overnight and denoted as Cu-Co_{t=x°C} as a final LDH catalyst.

3.2. Characterization

The BET surface area, pore volume, average pore size, and pore size distribution of samples were calculated from the isotherms of the N₂-physisorption, which is measured on a Micromeritics ASAP 2460 instrument by N₂ adsorption-desorption isotherms at −196 °C. All samples were dried at 50 °C for 72 h in a vacuum oven and then degassed at 50 °C for 72 h by nitrogen before measurements. The specific surface areas were calculated from the isotherms using Brunauer-Emmett-Teller (BET) method, and the pore size distributions were calculated by the Barrett-Joyner-Halenda (BJH) method.

Transmission electron microscopy (TEM) images were recorded on a TEM FEI Talos apparatus operating at acceleration voltage of 200 kV.

X-ray diffraction (XRD) was performed on a Bruker D8-Advance X-ray powder diffractometer with a Cu K α ray source ($\lambda = 0.154056 \text{ \AA}$) at 40 kV and 40 mA. The intensity data were collected at room temperature in a 2θ range from 10° to 70° with a scan rate of 6°/min.

Fourier transform infrared spectra (FT-IR) experiments were carried out on a FT-IR/ATR spectrophotometer (Nicolet 50, Thermo Fisher, Waltham, MA, USA). The spectra were collected from 4000 to 500 cm^{-1} with 32 scans and a resolution of 4 cm^{-1} .

X-ray photoelectron spectroscopy (XPS, ESCALAB 250Xi, Thermo Fisher) was investigated with a source of Al-K α radiation (1486.6 eV, a pass energy of 30.0 eV). C1s peak at 284.8 eV was used for calibration of all binding energies. The peaks were fitted according to references for O1s [31].

Laser Raman spectra (LRS) were collected on a confocal Raman (LabRam HR Evolution, Horiba, Kyoto, Japan) with a 50X objective under the excitation laser of 785 nm in ambient environment. Laser intensity was set as 3.2% ND Filter with 100 s acquisition time to ensure no damage of samples was caused during the experiment.

Diffuse reflectance UV-vis spectra in the range of 200–800 nm was recorded on an UV-3600 Plus (Shimadzu, Kyoto, Japan) spectrophotometer with BaSO₄ as reference.

3.3. Catalytic Performance Test

As for the catalytic activity, 10 mg of catalyst was dispersed in 100 mL of a 10-ppm RhB solution with a stirring rate of 700 rpm at 40 °C. The suspensions were first mixed for 1 h at a certain reaction temperature 40 °C to reach an adsorption-desorption equilibrium before H₂O₂ was added. Then, a 30 min Fenton-like reaction was activated by a dosage of 240 ppm H₂O₂ with an initial pH surrounding unless otherwise specified. Then, 3 mL of the liquid sample was taken from the reaction mixture at a given time and filtrated through a 0.22 μm Nafion membrane for the analysis of the RhB concentration by a UV-Vis spectrophotometer (UV-2600, Shimadzu, Kyoto, Japan) at an absorption wavelength of 554 nm. The RhB removal rate can be calculated by the following equation:

$$\text{RhB removal rate (\%)} = \frac{c_0 - c_t}{c_0} \times 100\% \quad (8)$$

where C_0 is the initial concentration of RhB, and C_t is the concentration of RhB at time t .

3.4. The Homogeneous Experiment

After the catalytic performance test, the metal ion concentration of the catalyst leached in the reaction solution was obtained by an atomic absorbance spectrometry (TAS-990F, Beijing Purkinje, Beijing, China) instrument. The conditions for the homogeneous experiment and the catalytic performance test were almost the same; the only difference is that equivalent metal nitrate salts were used as the catalyst in the homogeneous experiment.

3.5. The Quenching Test

The conditions for the quenching test and the catalytic performance test were also almost the same; the only difference is that an additional 50 mL of tert-butanol was added at the beginning of the experiment for the quenching test.

4. Conclusions

In this work, a novel Fenton-like catalyst, Co–Cu LDH, was prepared under different synthesis temperatures, and its best performance was achieved at a temperature of 65 °C. The superior catalytic activity can be attributed to the catalyst's structural defects, resulting from Cu doping, and Co–O–Cu in MO₆ surroundings enhanced the generation of Ov. Moreover, the high density of Ov under a strong Co–Cu interaction could improve the adsorption and dissociation of H₂O₂ as well as electron transfer to generate more ·OH, giving rise to increased RhB removal. Furthermore, the investigation of reaction parameters depicted the high catalytic activity of Co–Cu_{t=65°C}, which showed the highest removal, 96.2% RhB removal, in the first 5 min, with an H₂O₂ dosage of 480 ppm. The results indicate that the Co–Cu LDH catalyst is an attractive alternative organic pollutants treatment.

Author Contributions: Conceptualization and supervision, B.M.; methodology, validation, writing—original draft preparation, R.Z.; writing—review and editing, Y.L. and X.J.; All authors have read and agreed to the published version of the manuscript.

Funding: This research was funded by the Youth Program of the National Natural Science Foundation of China (Grant No. 21606209).

Data Availability Statement: Not applicable.

Conflicts of Interest: The authors declare no conflict of interest.

References

1. Rochat, J.; Demenge, P.; Rerat, J.C. Toxicologic study of a fluorescent tracer: Rhodamine B. *Toxicol. Eur. Res.* **1978**, *1*, 23–26. [[PubMed](#)]
2. Jain, R.; Mathur, M.; Sikarwar, S.; Mittal, A. Removal of the hazardous dye rhodamine B through photocatalytic and adsorption treatments. *J. Environ. Manag.* **2007**, *85*, 956–964. [[CrossRef](#)] [[PubMed](#)]
3. Namasivayam, C.; Sangeetha, D.; Gunasekaran, R. Removal of Anions, Heavy Metals, Organics and Dyes from Water by Adsorption onto a New Activated Carbon from Jatropha Husk, an Agro-Industrial Solid Waste. *Process Saf. Environ. Prot.* **2007**, *85*, 181–184. [[CrossRef](#)]
4. Purkait, M.K.; Maiti, A.; DasGupta, S.; De, S. Removal of congo red using activated carbon and its regeneration. *J. Hazard. Mater.* **2007**, *145*, 287–295. [[CrossRef](#)]
5. Javaid, R.; Qazi, U.Y.; Ikhlaq, A.; Zahid, M.; Alazmi, A. Subcritical and supercritical water oxidation for dye decomposition. *J. Environ. Manag.* **2021**, *290*, 112605. [[CrossRef](#)]
6. Javaid, R.; Qazi, U.Y.; Kawasaki, S. Highly efficient decomposition of Remazol Brilliant Blue R using tubular reactor coated with thin layer of PdO. *J. Environ. Manag.* **2016**, *180*, 551–556. [[CrossRef](#)]
7. Kim, S.C.; Lee, D.K. Preparation of Al-Cu pillared clay catalysts for the catalytic wet oxidation of reactive dyes. *Catal. Today* **2004**, *97*, 153–158. [[CrossRef](#)]
8. Hua, L.; Ma, H.R.; Zhang, L. Degradation process analysis of the azo dyes by catalytic wet air oxidation with catalyst CuO/ γ -Al₂O₃. *Chemosphere* **2013**, *90*, 143–149. [[CrossRef](#)]
9. Park, H.O.; Oh, S.; Bade, R.; Shin, W.S. Application of A2O moving-bed biofilm reactors for textile dyeing wastewater treatment. *Korean J. Chem. Eng.* **2010**, *27*, 893–899. [[CrossRef](#)]
10. Cripps, C.; Bumpus, J.A.; Aust, S.D. Biodegradation of Azo and Heterocyclic Dyes by Phanerochaete-Chrysosporium. *Appl. Environ. Microbiol.* **1990**, *56*, 1114–1118. [[CrossRef](#)]
11. Naeimi, A.; Sharifi, A.; Montazerghaem, L.; Abhari, A.R.; Mahmoodi, Z.; Bakr, Z.H.; Soldatov, A.V.; Ali, G.A.M. Transition metals doped WO₃ photocatalyst towards high efficiency decolourization of azo dye. *J. Mol. Struct.* **2022**, *1250*, 131800. [[CrossRef](#)]
12. Solehudin, M.; Sirimahachai, U.; Ali, G.A.M.; Chong, K.F.; Wongnawa, S. One-pot synthesis of isotype heterojunction g-C₃N₄-MU photocatalyst for effective tetracycline hydrochloride antibiotic and reactive orange 16 dye removal. *Adv. Powder Technol.* **2020**, *31*, 1891–1902. [[CrossRef](#)]
13. Wu, Y.; Zhou, S.; Qin, F.; Zheng, K.; Ye, X. Modeling the oxidation kinetics of Fenton's process on the degradation of humic acid. *J. Hazard. Mater.* **2010**, *179*, 533–539. [[CrossRef](#)]
14. Zhang, L.; Nie, Y.; Hu, C.; Qu, J. Enhanced Fenton degradation of Rhodamine B over nanoscaled Cu-doped LaTiO₃ perovskite. *Appl. Catal. B Environ.* **2012**, *125*, 418–424. [[CrossRef](#)]
15. Babuponnusami, A.; Muthukumar, K. A review on Fenton and improvements to the Fenton process for wastewater treatment. *J. Environ. Chem. Eng.* **2014**, *2*, 557–572. [[CrossRef](#)]
16. Lyu, L.; Yan, D.B.; Yu, G.F.; Cao, W.R.; Hu, C. Efficient Destruction of Pollutants in Water by a Dual-Reaction Center Fenton-like Process over Carbon Nitride Compounds-Complexed Cu(II)-CuAlO₂. *Environ. Sci. Technol.* **2018**, *52*, 4294–4304. [[CrossRef](#)]
17. Zhu, Y.P.; Ren, T.Z.; Yuan, Z.Y. Hollow cobalt phosphonate spherical hybrid as high-efficiency Fenton catalyst. *Nanoscale* **2014**, *6*, 11395–11402. [[CrossRef](#)]
18. Dai, C.; Tian, X.; Nie, Y.; Lin, H.M.; Yang, C.; Han, B.; Wang, Y. Surface Facet of CuFeO₂ Nanocatalyst: A Key Parameter for H₂O₂ Activation in Fenton-Like Reaction and Organic Pollutant Degradation. *Environ. Sci. Technol.* **2018**, *52*, 6518–6525. [[CrossRef](#)]
19. Khan, A.; Liao, Z.; Liu, Y.; Jawad, A.; Ifthikar, J.; Chen, Z. Synergistic degradation of phenols using peroxymonosulfate activated by CuO-CO₃O₄@MnO₂ nanocatalyst. *J. Hazard Mater.* **2017**, *329*, 262–271. [[CrossRef](#)]
20. Okamura, J.; Nishiyama, S.; Tsuruya, S.; Masai, M. Formation of Cu-supported mesoporous silicates and aluminosilicates and liquid-phase oxidation of benzene catalyzed by the Cu-mesoporous silicates and aluminosilicates. *J. Mol. Catal. A Chem.* **1998**, *135*, 133–142. [[CrossRef](#)]
21. Zhang, Y.; Liu, C.; Xu, B.; Qi, F.; Chu, W. Degradation of benzotriazole by a novel Fenton-like reaction with mesoporous Cu/MnO₂: Combination of adsorption and catalysis oxidation. *Appl. Catal. B Environ.* **2016**, *199*, 447–457. [[CrossRef](#)]
22. Anantharaj, S.; Karthick, K.; Kundu, S. Evolution of layered double hydroxides (LDH) as high performance water oxidation electrocatalysts: A review with insights on structure, activity and mechanism. *Mater. Today Energy* **2017**, *6*, 1–26. [[CrossRef](#)]

23. Wang, Y.; Yan, D.; El Hankari, S.; Zou, Y.; Wang, S. Recent Progress on Layered Double Hydroxides and Their Derivatives for Electrocatalytic Water Splitting. *Adv. Sci.* **2018**, *5*, 1800064. [[CrossRef](#)] [[PubMed](#)]
24. Navalon, S.; Alvaro, M.; Garcia, H. Heterogeneous Fenton catalysts based on clays, silicas and zeolites. *Appl. Catal. B Environ.* **2010**, *99*, 1–26. [[CrossRef](#)]
25. Cavani, F.; Trifirò, F.; Vaccari, A. Hydrotalcite-type anionic clays: Preparation, properties and applications. *Catal. Today* **1991**, *11*, 173–301. [[CrossRef](#)]
26. Guan, Y.-H.; Ma, J.; Li, X.-C.; Fang, J.-Y.; Chen, L.-W. Influence of pH on the Formation of Sulfate and Hydroxyl Radicals in the UV/Peroxymonosulfate System. *Environ. Sci. Technol.* **2011**, *45*, 9308–9314. [[CrossRef](#)]
27. Liu, Y.; Yang, J.; Guan, Q.; Yang, L.; Liu, H.; Zhang, Y.; Wang, Y.; Wang, D.; Lang, J.; Yang, Y.; et al. Effect of annealing temperature on structure, magnetic properties and optical characteristics in Zn_{0.97}Cr_{0.03}O nanoparticles. *Appl. Surf. Sci.* **2010**, *256*, 3559–3562. [[CrossRef](#)]
28. Nava-Andrade, K.; Carbajal-Arízaga, G.G.; Obregón, S.; Rodríguez-González, V. Layered double hydroxides and related hybrid materials for removal of pharmaceutical pollutants from water. *J. Environ. Manag.* **2021**, *288*, 112399. [[CrossRef](#)]
29. Li, H.; Shang, J.; Yang, Z.; Shen, W.; Ai, Z.; Zhang, L. Oxygen Vacancy Associated Surface Fenton Chemistry: Surface Structure Dependent Hydroxyl Radicals Generation and Substrate Dependent Reactivity. *Environ. Sci. Technol.* **2017**, *51*, 5685–5694. [[CrossRef](#)]
30. Jin, H.; Tian, X.; Nie, Y.; Zhou, Z.; Yang, C.; Li, Y.; Lu, L. Oxygen Vacancy Promoted Heterogeneous Fenton-like Degradation of Ofloxacin at pH 3.2–9.0 by Cu Substituted Magnetic Fe₃O₄@FeOOH Nanocomposite. *Environ. Sci. Technol.* **2017**, *51*, 12699–12706. [[CrossRef](#)]
31. Liu, P.F.; Yang, S.; Zhang, B.; Yang, H.G. Defect-Rich Ultrathin Cobalt–Iron Layered Double Hydroxide for Electrochemical Overall Water Splitting. *ACS Appl. Mater. Interfaces* **2016**, *8*, 34474–34481. [[CrossRef](#)]
32. Wang, H.; Zhang, Z.; Jing, M.; Tang, S.; Wu, Y.; Liu, W. Synthesis of CuNiSn LDHs as highly efficient Fenton catalysts for degradation of phenol. *Appl. Clay Sci.* **2020**, *186*, 105433. [[CrossRef](#)]
33. Tao, X.; Yang, C.; Wei, Z.; Huang, L.; Chen, J.; Cong, W.; Xie, R.; Xu, D. Synergy between Fenton process and DBD for methyl orange degradation. *Mater. Res. Bull.* **2019**, *120*, 110581. [[CrossRef](#)]
34. Lu, H.; Zhu, Z.; Zhang, H.; Zhu, J.; Qiu, Y.; Zhu, L.; Küppers, S. Fenton-Like Catalysis and Oxidation/Adsorption Performances of Acetaminophen and Arsenic Pollutants in Water on a Multimetal Cu-Zn-Fe-LDH. *ACS Appl. Mater. Interfaces* **2016**, *8*, 25343–25352. [[CrossRef](#)]
35. Guo, X.X.; Hu, T.T.; Meng, B.; Sun, Y.; Han, Y.-F. Catalytic degradation of anthraquinones-containing H₂O₂ production effluent over layered Co-Cu hydroxides: Defects facilitating hydroxyl radicals generation. *Appl. Catal. B Environ.* **2020**, *260*, 118157. [[CrossRef](#)]
36. Zeng, H.C.; Xu, Z.P.; Qian, M. Synthesis of Non-Al-Containing Hydrotalcite-like Compound Mg_{0.3}CoII_{0.6}CoIII_{0.2}(OH)₂(NO₃)_{0.2}·H₂O. *Chem. Mater.* **1998**, *10*, 2277–2283. [[CrossRef](#)]
37. Zhao, X.; Niu, C.; Zhang, L.; Guo, H.; Wen, X.; Liang, C.; Zeng, G. Co-Mn layered double hydroxide as an effective heterogeneous catalyst for degradation of organic dyes by activation of peroxymonosulfate. *Chemosphere* **2018**, *204*, 11–21. [[CrossRef](#)]
38. Liu, Q.; Wang, L.-C.; Chen, M.; Cao, Y.; He, H.-Y.; Fan, K.-N. Dry citrate-precursor synthesized nanocrystalline cobalt oxide as highly active catalyst for total oxidation of propane. *J. Catal.* **2009**, *263*, 104–113. [[CrossRef](#)]
39. He, L.; Li, Z.; Zhang, Z. Rapid, low-temperature synthesis of single-crystalline Co₃O₄ nanorods on silicon substrates on a large scale. *Nanotechnology* **2008**, *19*, 4–15. [[CrossRef](#)]
40. Zhang, R.; Zhang, Y.-C.; Pan, L.; Shen, G.-Q.; Mahmood, N.; Ma, Y.-H.; Shi, Y.; Jia, W.; Wang, L.; Zhang, X.; et al. Engineering Cobalt Defects in Cobalt Oxide for Highly Efficient Electrocatalytic Oxygen Evolution. *ACS Catal.* **2018**, *8*, 3803–3811. [[CrossRef](#)]
41. Lou, Y.; Ma, J.; Cao, X.; Wang, L.; Dai, Q.; Zhao, Z.; Cai, Y.; Zhan, W.; Guo, Y.; Hu, P.; et al. Promoting Effects of In₂O₃ on Co₃O₄ for CO Oxidation: Tuning O₂ Activation and CO Adsorption Strength Simultaneously. *ACS Catal.* **2014**, *4*, 4143–4152. [[CrossRef](#)]
42. Wang, X.F.; Xu, J.B.; Zhang, B.; Yu, H.G.; Wang, J.; Zhang, X.; Yu, J.G.; Li, Q. Signature of Intrinsic High-Temperature Ferromagnetism in Cobalt-Doped Zinc Oxide Nanocrystals. *Adv. Mater.* **2006**, *18*, 2476–2480. [[CrossRef](#)]
43. Gandhi, V.; Ganesan, R.; Abdulrahman Syedahamed, H.H.; Thaiyan, M. Effect of Cobalt Doping on Structural, Optical, and Magnetic Properties of ZnO Nanoparticles Synthesized by Coprecipitation Method. *J. Phys. Chem. C* **2014**, *118*, 9715–9725. [[CrossRef](#)]
44. Bao, J.; Zhang, X.; Fan, B.; Zhang, J.; Zhou, M.; Yang, W.; Hu, X.; Wang, H.; Pan, B.; Xie, Y. Ultrathin Spinel-Structured Nanosheets Rich in Oxygen Deficiencies for Enhanced Electrocatalytic Water Oxidation. *Angew. Chem. Int. Ed. Engl.* **2015**, *54*, 7399–7404. [[CrossRef](#)] [[PubMed](#)]
45. Parida, K.; Mohapatra, L.; Baliarsingh, N. Effect of Co²⁺-Substitution in the Framework of Carbonate Intercalated Cu/Cr LDH on Structural, Electronic, Optical, and Photocatalytic Properties. *J. Phys. Chem. C* **2012**, *116*, 22417–22424. [[CrossRef](#)]
46. Godelitsas, A.; Charistos, D.; Tsipis, C.; Misaelides, P.; Filippidis, A.; Schindler, M. Heterostructures patterned on aluminosilicate microporous substrates: Crystallization of cobalt(III) tris(N,N-diethyldithiocarbamate) on the surface of a HEU-type zeolite. Microporous and Mesoporous. *Materials* **2003**, *61*, 69–77. [[CrossRef](#)]
47. Khassin, A.A.; Anufrienko, V.F.; Ikorskii, V.N.; Plyasova, L.M.; Kustova, G.N.; Larina, T.V.; Molina, I.Y.; Parmon, V.N. Physico-chemical study on the state of cobalt in a precipitated cobalt-aluminum oxide system. *Phys. Chem. Chem. Phys.* **2002**, *4*, 4236–4243. [[CrossRef](#)]

48. Li, X.; Dai, Y.; Ma, Y.; Huang, B. Electronic and magnetic properties of honeycomb transition metal monolayers: First-principles insights. *Phys. Chem. Chem. Phys.* **2014**, *16*, 13383–13389. [[CrossRef](#)]
49. Lin, W.Y.; Frei, H. Anchored metal-to-metal charge-transfer chromophores in a mesoporous silicate sieve for visible-light activation of titanium centers. *J. Phys. Chem. B* **2005**, *109*, 4929–4935. [[CrossRef](#)]
50. Mohapatra, L.; Parida, K.M. Dramatic activities of vanadate intercalated bismuth doped LDH for solar light photocatalysis. *Phys. Chem. Chem. Phys.* **2014**, *16*, 16985–16996. [[CrossRef](#)]
51. Nakamura, R.; Okamoto, A.; Osawa, H.; Irie, H.; Hashimoto, K. Design of all-inorganic molecular-based photocatalysts sensitive to visible light: Ti(IV)-O-Ce(III) bimetallic assemblies on mesoporous silica. *J. Am. Chem. Soc.* **2007**, *129*, 9596. [[CrossRef](#)] [[PubMed](#)]
52. Nayak, S.; Mohapatra, L.; Parida, K. Visible light-driven novel g-C₃N₄/NiFe-LDH composite photocatalyst with enhanced photocatalytic activity towards water oxidation and reduction reaction. *J. Mater. Chem. A* **2015**, *3*, 18622–18635. [[CrossRef](#)]
53. Xu, D.; Sun, X.; Zhao, X.; Huang, L.; Qian, Y.; Tao, X.; Guo, Q. Heterogeneous Fenton Degradation of Rhodamine B in Aqueous Solution Using Fe-Loaded Mesoporous MCM-41 as Catalyst. *Water Air Soil Pollut.* **2018**, *229*, 317. [[CrossRef](#)]
54. Han, X.; Zhang, H.; Chen, T.; Zhang, M.; Guo, M. Facile synthesis of metal-doped magnesium ferrite from saprolite laterite as an effective heterogeneous Fenton-like catalyst. *J. Mol. Liq.* **2018**, *272*, 43–52. [[CrossRef](#)]
55. Sheng, Y.; Sun, Y.; Xu, J.; Zhang, J.; Han, Y.-F. Fenton-like degradation of rhodamine B over highly durable Cu-embedded alumina: Kinetics and mechanism. *AIChE J.* **2018**, *64*, 538–549. [[CrossRef](#)]
56. Phan, T.T.N.; Nikoloski, A.N.; Bahri, P.A.; Li, D. Enhanced removal of organic using LaFeO₃-integrated modified natural zeolites via heterogeneous visible light photo-Fenton degradation. *J. Environ. Manag.* **2019**, *233*, 471–480. [[CrossRef](#)]
57. Vu, A.-T.; Xuan, T.N.; Lee, C.-H. Preparation of mesoporous Fe₂O₃-SiO₂ composite from rice husk as an efficient heterogeneous Fenton-like catalyst for degradation of organic dyes. *J. Water Process. Eng.* **2019**, *28*, 169–180. [[CrossRef](#)]
58. Abdullah, A.Z.; Ling, P.Y. Heat treatment effects on the characteristics and sonocatalytic performance of TiO₂ in the degradation of organic dyes in aqueous solution. *J. Hazard. Mater.* **2010**, *173*, 159–167. [[CrossRef](#)]
59. Sun, Y.; Yang, Z.; Tian, P.; Sheng, Y.; Xu, J.; Han, Y.-F. Oxidative degradation of nitrobenzene by a Fenton-like reaction with Fe-Cu bimetallic catalysts. *Appl. Catal. B Environ.* **2019**, *244*, 1–10. [[CrossRef](#)]
60. Herney-Ramirez, J.; Vicente, M.A.; Madeira, L.M. Heterogeneous photo-Fenton oxidation with pillared clay-based catalysts for wastewater treatment: A review. *Appl. Catal. B Environ.* **2010**, *98*, 10–26. [[CrossRef](#)]
61. Liu, Y.; Zhang, J.; Yin, Y. Removal of Hg⁰ from flue gas using two homogeneous photo-fenton-like reactions. *AIChE J.* **2015**, *61*, 1322–1333. [[CrossRef](#)]
62. Ding, R.R.; Li, W.Q.; He, C.S.; Wang, Y.R.; Liu, X.C.; Zhou, G.N.; Mu, Y. Oxygen vacancy on hollow sphere CuFe₂O₄ as an efficient Fenton-like catalysis for organic pollutant degradation over a wide pH range. *Appl. Catal. B Environ.* **2021**, *291*, 120069. [[CrossRef](#)]
63. Pignatello, J.J.; Oliveros, E.; MacKay, A. Advanced oxidation processes for organic contaminant destruction based on the Fenton reaction and related chemistry (vol 36, pg 1, 2006). *Crit. Rev. Environ. Sci. Technol.* **2007**, *37*, 273–275.
64. Zhang, N.; Li, X.; Ye, H.; Chen, S.; Ju, H.; Liu, D.; Lin, Y.; Ye, W.; Wang, C.; Xu, Q.; et al. Oxide Defect Engineering Enables to Couple Solar Energy into Oxygen Activation. *J. Am. Chem. Soc.* **2016**, *138*, 8928–8935. [[CrossRef](#)]
65. Cahill, A.E.; Taube, H. The Use of Heavy Oxygen in the Study of Reactions of Hydrogen Peroxide. *J. Am. Chem. Soc.* **1952**, *74*, 2312–2318. [[CrossRef](#)]
66. Dixon, W.T.; Norman, R.O.C. Free radicals formed during the oxidation and reduction of peroxides. *Nature* **1962**, *196*, 891–892. [[CrossRef](#)]